Journal of Oncology Research and Therapy
Pesnel S, et al. Oncol Res Ther 9: 10244.
www.doi.org/10.29011/2574-710X.10244
www.gavinpublishers.com

OPEN ACCESS

GAVIN PUBLISHERS

Research Article

Preclinical Assessment of Metallic Nanotheranostics for Pancreatic and Prostatic Carcinoma: Sustainable Synthesis and Biodistribution Study

Pesnel S[1], Chave T[2], Grimaud A[2], Nikitenko SI[2*], Morel AL[1,3*]

[1]Torskal, 2 Rue Maxime Rivière, 97490 Sainte-Clotilde, La Réunion, France

[2]ICSM, Univ Montpellier, CEA, CNRS, ENSCM, Marcoule, France

[3]Suzhou Anne Gold Nano Biotechnology Co., LTD, Suzhou Nano Health Industrial Park, China

***Corresponding author:** Morel AL, Torskal, 2 Rue Maxime Rivière, 97490 Sainte-Clotilde, La Réunion, France.

Nikitenko SI, ICSM, Univ Montpellier, CEA, CNRS, ENSCM, Marcoule, France.

Citation: Pesnel S, Chave T, Grimaud A, Nikitenko SI, Morel AL (2024) Preclinical Assessment of Metallic Nanotheranostics for Pancreatic and Prostatic Carcinoma: Sustainable Synthesis and Biodistribution Study. J Oncol Res Ther 9: 10244. DOI: 10.29011/2574-710X.10244.

Received Date: 25 August, 2024; **Accepted Date:** 03 September, 2024; **Published Date:** 05 September, 2024

Abstract

Metallic nanoparticles present interesting properties for imaging and therapeutic applications in oncology. We described the synthesis of core-shell gold-iron oxide nanoparticles, designed by green chemistry, in theranostic application. Core-shell Fe_3O_4@Au nanoparticles integrate the magnetic characteristics of the Fe_3O_4 core with the distinct properties of metallic gold, resulting in a multifunctional agent for therapeutic applications. **Objectives:** The assessment of the MRI contrast agent and radiosensitizer properties of hybrid nanoparticles. **Methods:** We assessed the toxicity of the hybrid nanoparticles (NP) on tumor cells, the effects of NP stimulated by X-rays radiations, their properties as T2 contrast agent for MRI and their biodistribution. **Results:** Herein, we report a sustainable protocol to synthesize by green chemistry core-shell nanoparticles Fe_3O_4@Au involving 3 consecutive steps: (i) ultrasonically assisted synthesis of monodispersed 7-8 nm magnetite nanoparticles (ii) adsorption of L-Cysteine to the Fe_3O_4 nanoparticles, and (iii) reductive deposition of the uniform gold shell on Fe_3O_4/L-Cysteine precursor under controlled conditions. The obtained core-shell nanoparticles exhibit distinct magnetic properties (Ms = 48 emu·g-1, Hc = 6 mT). The functionalization of nanoparticles either by neurotensin or by AMD 3100 reported different profile of biodistribution. Finally, we reported the radioenhancement property of these NP for the treatment of pancreatic adenocarcinoma and prostatic carcinoma and to act as T2 contrast agent for medical imaging. The physicochemical properties and the biodistribution profile suggest that the intratumoral injection would be the best way to accumulate the nanoparticles in the targeted tissue.

Keywords: Nanoparticles; Radiosensitizer; Radiotherapy; Prostate Carcinoma; Pancreatic Adenocarcinoma; Biodistribution;

Introduction

The phenomenon of dose enhancement at interfaces between materials with high and low atomic numbers (Z) has been explored for over five decades [1]. This effect was responsible for causing burns and necrosis in tissues surrounding reconstructive wires in mandibular cancer patients following radiation therapy [2]. Over 20 years ago, Matsudaira et al. [3] proposed the use of high-Z materials to enhance dose delivery in cancer radiotherapy.

High atomic number metal nanostructures, such as gold and platinum, have been identified as promising photoabsorbent or photosensitizing agents when used with laser or X-ray beams in photothermal therapy and radiotherapy [4, 5]. This has led to significant interest in iron oxide/gold composite magnetic nanoparticles over the past several decades [6-8]. Gold, in particular, is an excellent X-ray absorber [4]. Loading tumors with gold can result in a significantly higher radiation dose to cancerous tissue compared to the dose received by surrounding normal tissue during radiotherapy. Calculations suggest that this dose enhancement could be substantial, potentially increasing by 200% or more.

Radiotherapy continues to be a cornerstone of cancer treatment. Advances such as the use of megavolt (6–25 MV) X-rays to minimize skin damage, tomotherapy, and intensity-modulated radiation therapy (IMRT) to better conform the dose to the tumor shape, as well as improved dose fractionation schedules, have improved outcomes. However, radiotherapy may still fail to completely eliminate tumors due to factors such as radioresistant tumor cells (e.g., hypoxic cells), under-irradiated areas, or cells outside the targeted region. Generally, mitotically active tumor tissues are only slightly more sensitive to radiation than essential normal tissues, including those in the gastrointestinal mucosae, lungs, brain, bone marrow, and lymphoid tissues. Infiltrative cancers, particularly those in the nervous system, neck, and intestines, present a particular challenge. Another limitation of radiation therapy is the cumulative nature of cellular damage. DNA strand breaks or other cell damage that are not repaired may not kill a normal cell immediately, but further irradiation adds to the damage, eventually leading to cell death. This cumulative effect means that a tumor-controlling dose, which inevitably damages surrounding normal tissue, cannot be administered at the same level in subsequent treatments (e.g., six months later if the tumor regrows), making it increasingly difficult to control the disease.

Despite the impressive progress of therapies, some cancers like pancreatic adenocarcinoma remain difficult to treat [5]. A therapeutic option is the use of radiation therapy. High doses of X- rays radiations are used to kill cancer cells and shrink tumors. Unfortunately, sometimes, delivered doses cannot be as high as necessary because of the exposure of surrounding tissues. X-rays radiations cross healthy tissues before reaching tumor cells, so the delivered doses inside these tissues must be as low as possible.

A strategy to enhance the radiation dose within a tumor while minimizing exposure to surrounding healthy tissue involves combining X-ray radiation with metallic nanoparticles containing high-Z atoms [6-11]. When low-energy photons interact with these metals, they trigger the release of photoelectrons and Auger electrons, resulting in localized dose enhancement and the production of reactive oxygen species (ROS) that can damage nearby cells.

The mainstream approach for synthesizing such hybrid nanoparticles is to first create the iron oxide core, then complete it with the gold deposition using various Au(III) reducing reagents [12-14]. However, in most cases the gold shell on the Fe_3O_4 surface is not really uniform, which can lead to the dissolution of the iron oxide in biological fluids containing complexing ligands through the junctions between Au nanoparticles. In addition, many reducing reagents used in these studies are not really biocompatible.

Wagener et al. introduced a unique approach for synthesizing Fe_3O_4@Au magnetic nanoparticles by employing pulsed laser ablation of an FeAu alloy in various solvents [15]. This technique leads to quite large polydispersed particles (70-90 nm) with a ca. 20 nm uniform gold shell. Narayanan et al. have employed grape seed proanthocyanidin as a green reducing reagent [16]. Morphological characterisation proved a core-satellite nanohybrid formation with a quasi-spherical ca. 30 nm Fe_3O_4 core with ca. 2 nm Au NPs attached to its surface. Furthermore, using a large excess of proanthocyanidin during synthesis can result in the reduction of Au(III) not only on the surface of Fe3O4 but also in the bulk solution. More in general, green chemistry approach for preparing Fe_3O_4@Au MNPs has been much less explored compared to the traditional synthetic methods.

This Paper Focused on:

*The radiotherapy enhancement using small iron oxide/gold-based nanoparticles. Gold is a biocompatible metal with a high atomic number (Z=79). Iron oxide nanoparticles were already studies as radiosensitizers and demonstrated good properties and in addition, iron oxide is a T2 contrast agent for MRI [17-19].

These hybrid nanoparticles combine two metals, serving as dual-modality agents with both diagnostic (biocompatible contrast agent) and therapeutic (radiosensitizer) capabilities.

A three-stage green synthesis method has been developed to produce Fe_3O_4@Au magnetic nanoparticles with a uniform gold

shell:

1. Ultrasonically Assisted Preparation of Fe_3O_4 Nanoparticles: Previous studies have shown that coprecipitating Fe(II) and Fe(III) in alkaline solutions under 20 kHz ultrasound yields Fe_3O_4 nanoparticles with a narrow size distribution ranging from 4 to 8 nm.

2. Adsorption of L-Cysteine on Fe_3O_4 Nanoparticles: L-Cysteine is adsorbed onto the surface of Fe_3O_4 nanoparticles through coordination with carboxylate groups, leading to the formation of Cystine via SS bonding.

3. Reduction of Au(III) with Cystine on Fe_3O_4 Nanoparticles: Under carefully controlled conditions and without additional chemicals, Au(III) is reduced by Cystine at the surface of the Fe_3O_4 nanoparticles, resulting in the formation of a uniform gold shell.

Materials and Methods

Material

All Solids: HAuCl4 (99.995 % metal basis, Alfa Aesar), NaOH (>97%, Carlo Erba), FeCl2.4H2O (>99%, Honeywell Fluka), FeCl3.6H2O (97% ACS Reagent, Sigma Aldrich) and L-Cysteine hydrochloride hydrate (>99%, Aldrich) were purchased and used without further purification. All solutions were prepared using ultrapure water with resistivity of 18.2 MΩ.cm at 25 °C (Milli-Q system). Ar of 99.999% purity was supplied by Air Liquide. Certified potassium phthalate standard at 50 $mgC.L^{-1}$ for TOC measurement and ICP-OES gold standards at $1gAu.L^{-1}$ were purchased from VWR and SCP Science respectively.

Cells Culture

MIA PaCa-2 human pancreatic cancer cell line was purchased from the JCRB (Osaka, Japan) and DU145 human prostate cancer cell line was purchased from ATCC. These cell lines were cultured in DMEM supplemented with 10% heat-inactivated fetal bovine serum, 50 U/ml penicillin and 50 µg/ml streptomycin. The cell lines were maintained at 37°C in 5% CO2 and 95% air in a humidified atmosphere.

Metallic Nanoparticles Synthesis

Synthesis of Fe_3O_4 nanoparticles assisted by US

Fe_3O_4 NPs syntheses were performed by co-precipitation of Fe(II)/Fe(III) ions in alkaline medium within a 50 mL double jacket reactor under the assistance of 20 kHz ultrasonic irradiation (Sonics VCX750) as described previously [12]. This reactor is equipped with three sealed overtures allowing the control of the gas atmosphere and the regulation of the medium temperature thanks to a cryostat (Huber CC1). Experiments were carried out at 27±2 °C under argon gas atmosphere with a constant flow rate of 100 mL/min. Ultrasonic irradiation was achieved by a 1 cm² sonotrode tip immerged within the solution at a reproducible distance of 2 cm from the reactor bottom with an applied acoustic power of 19 $W.cm^{-2}$.

Sustainable Synthesis of Fe_3O_4@Au Nanoparticles

The synthesis was previously described in the patent [18].

Firsly, the synthesis of Fe_3O_4 nanoparticles was performed according to the method previously described by Morel et al. [17], by substituting hydrazine and ammonia by sonochemical approach to follow the principles of green chemistry.

In the second step of synthesis, a 0.05 M solution of L-cysteine (L-Cyst) was prepared by dissolving L-cysteine hydrochloride hydrate ($HSCH_2CH(NH_2)CO_2H$ - $xHCl$ - xH_2O) in pure water. A mass of 50 mg of Fe_3O_4 nanoparticles was dispersed in 40 mL of water for 10 min using an ultrasonic reactor. Then, 5 mL of L-Cyst was added to the suspension under continuous ultrasonic treatment for 5 minutes and the pH was adjusted to [6-7]. Then, the suspension was stirred by mechanical stirring for 65 h. After establishing sorption equilibrium, the particles were washed several times with distilled water. The separation of the particles after each wash was carried out with a permanent magnet. Finally, in the third step consisting in the deposition of the gold shell on the Fe_3O_4-L-Cysteine nanoparticles, 50 mg of Fe_3O_4-L-Cyst nanoparticles suspended in water were mixed with 40 mL of water and treated with ultrasound for 10 min. Then, this suspension was placed in the reactor with the mechanical stirrer and every 15 min 0.5 mL of HAuCl4 solution ($0.5\ g.L^{-1}$) was added under stirring up while maintening the pH between [6-7]. After 2h15 min of stirring, the suspension was removed from the reactor and washed twice with pure water.

X-ray Irradiation

Irradiations were done using a 6 MV Truebeam® linear accelerator (Varian medical systems®). All the samples were irradiated at 5 cm depth in solid water equivalent material at 100cm source-to-axis distance with a field size of 15 x 15 cm. 6 cm of water-equivalent back-scatter material were also placed on top of the samples (Figure 1).

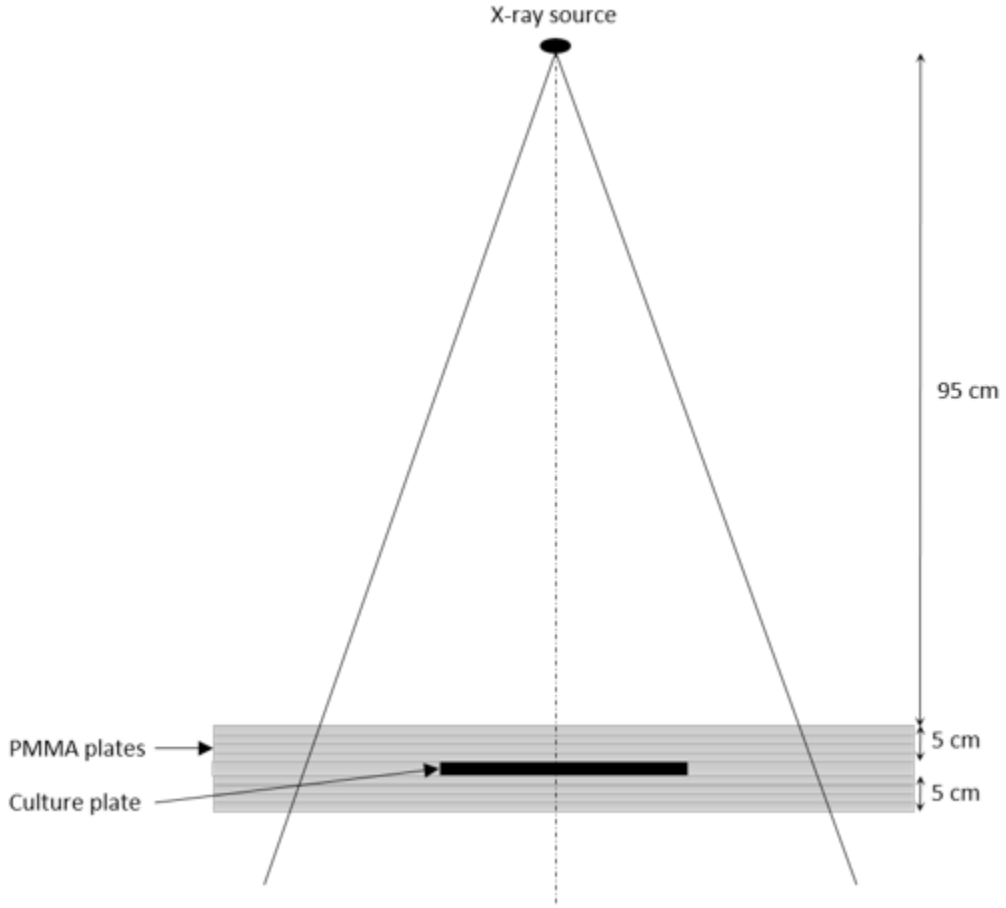

Figure 1: Schematic diagram of irradiation configuration.

Measurement of Cell Viability

Effects of NP on cell viability: MIA PaCa-2 and DU145 cells were plated at a density of 1 x 104 cells/well in 96-well plates and incubated overnight at 37% under 5% CO2. To determine the cytotoxicity of NP, cells were treated with a concentration range of NP for 24h. Cell growth inhibition was determined by measuring 3-(4,5-dimethylthiazol-2-yl)-2,5-diphenyltetrazolium bromide (MTT) dye absorbance by living cells. MTT solution (2.5 mg/mL in PBS) was added to each well and cells were incubated for 4h. Formazan crystals resulting from MTT reduction were dissolved by the addition of 10% SDS in DMSO/acetic acid solution per well. The relative quantity of formazan products formed in each well was detected by reading absorbance at 570 nm. Cell growth was normalized to a control group without any treatment.

Effects of NP coupled to X-ray irradiation on cell viability: MIA PacA-2 and DU145 cells pre- treated for 1h with 50 or 100 µg/ml NP and exposed to 2, 4 or 6 Gy radiation treatments were cultured at a density of 1 x 104 cells/well and incubated for 72h. Cell growth inhibition was determined by MTT assay.

Colony Formation Assay

MIA PaCa-2 and DU145 cells were plated at a density of 2 x 10^5 cells/well in 6-weel plates and incubated overnight at 37% under 5% CO2. Cells were then exposed for 1h to NP and irradiated with 0-6 Gy X-rays. 1 hour later, cells were washed, trypsinized, counted and replated in 6 well- plates and incubated for 9-14 days. Colonies were then fixed with methanol and stained with 0.1% crystal violet. The plates were washed and airdried, then colonies were counted.

Clonogenic survival was fitted according to a linear quadratic model of the form $SF = \exp(-\alpha D - \beta D^2)$, where SF is the surviving fraction, and a and ß represent the probabilities of lethal and sub-

lethal damage, respectively. The data were normalized to the plating efficiency (PE) of the control condition (0 Gray) using the following equations:

$$PE = \frac{\#\ of\ colonies\ formed}{\#\ of\ cells\ seeded}\ x\ 100$$

ROS Measurement

MIA PaCa-2 and DU145 cells were treated with NP (50 or 100 µg/ml) for 1h and exposed to X-ray irradiation (0 to 6 Gy). ROS were detected using an oxidation-sensitive fluorescent probe dye 2,7-dichlorodihydrofluorescein diacetate (H2DCFDA, 20 µM) for 30min. Fluorescence was acquired using a FLUOstar Omega system with the suitable filters.

Apoptosis Detection

MIA PaCa-2 and DU145 cells were treated with NP (50 or 100 µg/ml) for 1h and exposed to X-ray irradiation (0 to 6 Gy). 72h after irradiation, apoptosis was detected using Apo-ONE® homogeneous caspase-3/7 assay kit (Promega, France) following the manufacturer's instructions. Fluorescence was acquired using a FLUOstar Omega system with the suitable filters.

In vitro MR Imaging

In vitro MR imaging was carried out using a preclinical 4.7 T MRI scanner (Bruker BioSpec 4.7T). The NP solutions with concentrations from 0.1 to 0.76 mM were imaged using T1 and T2 sequences to determine the longitudinal relaxivity (r1) and the transversal relaxivity (r2). Relaxation rates (1/T1 and 1/T2, s-1) were plotted as a function of iron concentration, expressed in mM of iron, and the relaxivities (r1 and r2) were obtained by the slope of the fitting straight line.

Statistical Analysis

All experiments were carried out in triplicate with the results expressed as the mean ± standard deviation. Data were analyzed by One-Way Analysis of Variance (ANOVA) followed by post-hoc comparisons by Tukey's HSD test. All data were analysis using GraphPad Prism 8.0 package (GraphPad software, USA). Statistical significance is indicated as * $P<0.05$, ** $P<0.01$, *** $P<0.001$ and **** $P<0.0001$.

Biodistribution Study

Nanoparticles

Two different nanoparticles were synthesized for the biodistribution study on pancreatic mice model

Tumor Model	Ligands	Target
Pancreas	Neurotensin	Neurotensin Receptor (NTR1)
	AMD3100	CxCR4

Tumor Cell Line

MIA PaCa-2 (ATCC® CRL-1420TM) is a human pancreatic carcinoma cell line. Cell line were cultured in DMEM supplemented with FBS (10%), glucose (4,5g/L), sodium pyruvate, L-glutamine.

Mice

80 Balb/c nude mice, 6 weeks-old were used.

Orthotopic Model of Pancreatic Tumor

Abdomens were prepped with betadine solution. A 1-cm wide incision was made in the left upper quadrant of the abdomen. The tip of pancreatic tail was gently grasped and pancreas was externalized in a lateral direction to be fully exposed. 2.106 MIA PaCa-2 cells in 50 µL PBS was slowly injected using a 27-gauge needle inserted into the tail of pancreas and positioned in the pancreatic head region. The spleen was then returned to the appropriate position in abdomen, and skin and peritoneum was closed with 5-0 vicryl sutures or 9 mm staples. The animals were then placed on a warming blanket until they recovered from anesthesia.

Biodistribution Study

4 weeks after tumor cells injection, nanoparticles were injected to mice with different routes of administration (intratumor and intravenous).

- Intravenous injection: 200µL of nanoparticles were injected in the tail vein
- Intratumoral injection: a small incision was made in the left upper quadrant of the abdomen in order to externalize the spleen and the pancreas. Then 50µL of nanoparticles were injected into the tumor.

Mice were then sacrificed at different time post-injection (1h; 24h; 168h; 2 mice/time) and the main organs (tumor, spleen, liver, kidney, plasma) were removed, washed and weighed for ICP-MS quantitation. A sample of nanoparticles and a sample of blood was analyzed by ICP-MS. The gold concentrations in Au/kg sample were determined and gold concentrations per sample mass were calculated by determining the total gold content of each sample tube and dividing by the mass of each sample.

Nanoparticles	Administration Route	Number of Mice	Sacrifices and Organ Removal
NP@Neurotensin	Intravenous (50uL)	12	1h; 24 and 168h after injection (2 mice per time)
	Intratumor (200uL)	12	
NP@AMD3100	Intravenous (50uL)	12	
	Intratumor (200uL)	12	

Results

Synthesis of Fe_3O_4 Nanoparticles

In this work, Fe3O4 nanoparticles were obtained by ultrasonically assisted coprecipitation of Fe(II) and Fe(III) as it was reported in the literature [12]. The sonoreactor was equipped with a titanium ultrasonic probe and piezoelectric transducer supplied by a 20 kHz generator (Vibra Cell 600). The temperature in the reactor during ultrasonic treatment was maintained at 25 °C using a Huber Unistat Tango thermocryostate. Argon (< 1 ppm of O2) was bubbled at a rate of ca. 100 mL·min-1 prior and during the ultrasonic treatment. For each synthesis, 40 mL of 0.33 M NaOH solution were first introduced in the reactor. The ultrasonic irradiation was then applied to reach a steady state temperature of 25 °C. After 15 minutes, 10 mL of a freshly prepared mixture of 0.22 M Fe(III) and 0.11 M Fe(II) precursors was then injected with the help of a syringe directly within the cavitation zone. This Fe(III)/Fe(II) ratio ensure to obtain Fe_3O_4 NPs around 6±2 nm as previously reported within the literature [12]. The formation of the magnetite particles could be observed with the almost instant black coloration of the medium. The suspension was hold under sonication for additional 15 minutes. Finally, the magnetite particles were recovered with the help of permanent magnet and washed several times with deionized water until pH close to neutrality. Obtained samples were stored as aqueous suspensions in glass vials.

Adsorption of L-Cysteine on Magnetite Particles

L-Cysteine solutions were prepared just before use with a concentration of 0.05 M. The initial concentration of L-Cysteine was checked with the help of TOC-meter (Shimadzu TOC-VCSH) calibrated with potassium phthalate standards. For each batch, 250 mg of Fe_3O_4 particles were redispersed in 40 mL of pure water under low ultrasonic irradiation for 10 min (20 kHz, 19 W.cm-2). After ultrasonic treatment, 10 mL of 0.05 M L-Cysteine solution was added to the Fe3O4 aqueous suspension with a final total volume of 50 mL. The as prepared suspension was then sonicated once again for 5 min before being placed under mechanical stirring for 48 hours in a glass reactor. Since L-Cysteine adsorption on Fe_3O_4 surface is strongly pH dependent, the suspension pH was checked all over the procedure and adjusted to 6 by addition of 0.33 M NaOH solution [13]. The concentration of L-Cysteine in solution was monitored during the process by TOC measurements. As observed in Fig. 2, a plateau is reached after 17 hours of contact between the L-Cysteine solution and the magnetite particles with almost 80% of the initial L- Cysteine adsorbed. The Fe_3O_4/L-Cysteine suspension can be then recovered and washed several times with ultrapure water before gold deposition to minimize the amount of L-Cysteine remaining in bulk solution.

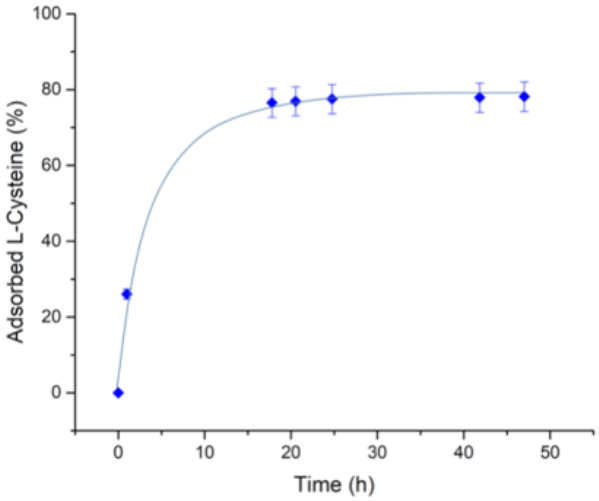

Figure 2: L-Cysteine adsorption kinetics on Fe_3O_4 MNPs at pH 6, 25 °C.

ATR-FTIR measurements on dried Fe_3O_4/L-Cysteine samples revealed the presence of three characteristic peaks at 1596, 1379 and 1068 cm-1 compared to bare Fe_3O_4 MNPs spectrum (Fig S1). According to the literature, the 1596 cm-1 and 1379 cm-1 absorption bands are respectively specific of the asymmetric and symmetric stretching of carbonyl group whereas the 1068 cm-1 peak could be attributed to C-N stretching [13]. These results therefore confirm the adsorption of L-Cysteine at the surface of the magnetite particles.

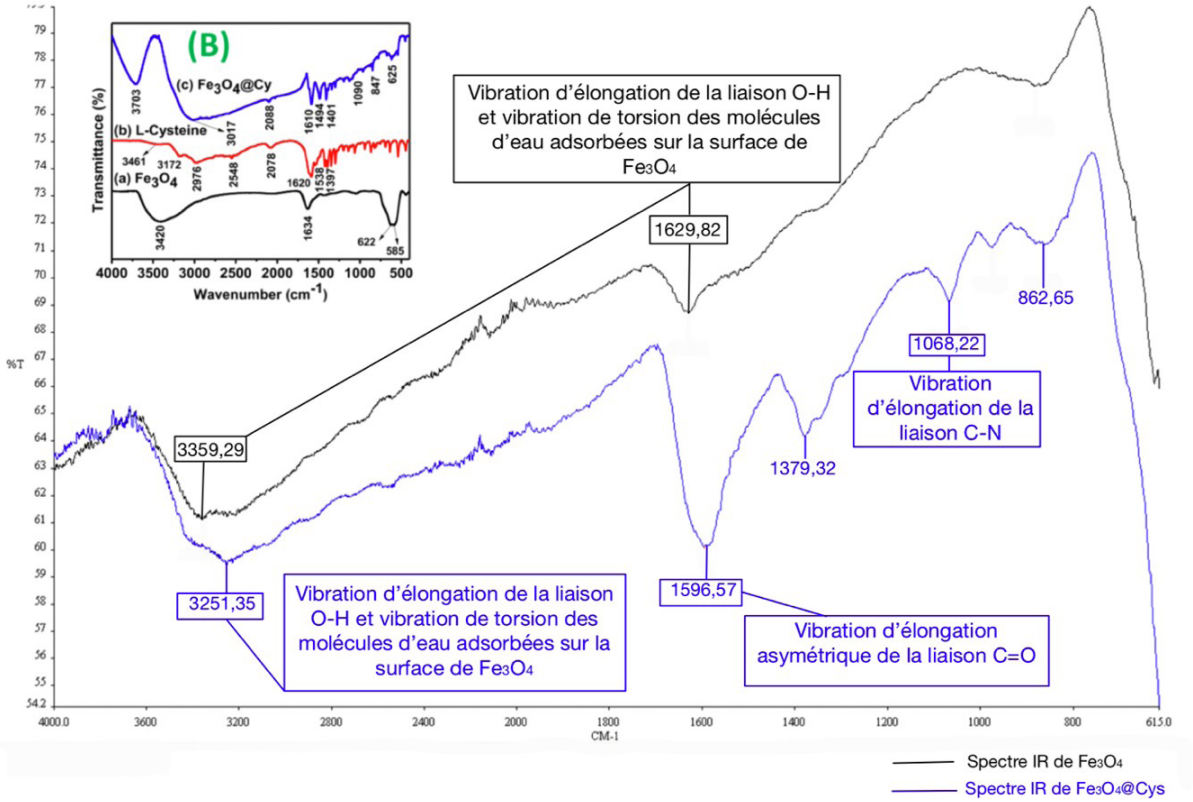

Figure S1: Comparison of IRTF spectra from Fe_3O_4 and Fe_3O_4@Cys in a solid state.

Deposition of Gold on Fe_3O_4 Nanoparticles

For this last step, previously obtained Fe_3O_4/L-Cysteine precursor was dispersed in ultrapure water within a total volume of 100 mL. The pH of initial suspension was controlled and adjusted if needed to a value close to neutrality and the sample was then sonicated for 10 minutes to guarantee the good dispersion of the particles. The suspension was then introduced within the same glass reactor as used for the L-Cysteine adsorption procedure under vigorous mechanical stirring of 300 rpm.

To ensure a progressive and homogeneous gold deposition on the magnetite particles, 0.55 mL of HAuCl4 solution (2.25 gAu.L^{-1}) was added every 10 minutes until reaching a total of 5 wt% of gold deposited on Fe3O4/L-Cysteine (calculated on pristine oxide basis). After each gold precursor addition, the pH of suspension was checked and kept as close as possible to a value of 6 with the help of sodium hydroxide solution. As reported in Fig. 2, ICP-OES analyses performed 5 minutes after the final HAuC [14] solution addition at different time confirmed the complete and fast reduction of gold since no Au(III) ions could be detected within the solution with a final reduction yield of 99.8 % (detection limit below 0.1 ppm). At the end of the experiment, the Fe_3O_4@Au suspension was recovered by magnetic separation and washed at least twice with ultrapure water to reach pH neutrality.

Structural and Morphological Characterization

Powder XRD patterns of Fe_3O_4 and Fe_3O_4@Au MNPs point out a spinel structure (Fig. 3) typical for magnetite. It is worth noting that γ-Fe2O3 has the same structure type; therefore, the presence of Fe_3O_4 in core-shell MNPs was confirmed using XPS described below. Au patterns are not observed in the XRD diagram of Fe_3O_4@Au MNPs most likely because of its low concentration. HRTEM image of L-Cysteine mediated Fe_3O_4@Au MNPs shown in Fig. 4 reveals monodispersed round-shaped 7-8 nm NPs in agreement with previously published data [17]. The core-shell structure of these NPs is clearly distinguishable as well. Roughly, the shell thickness is about 1 nm. Further study of Fe_3O_4@Au MNPs using STEM coupled with EDX analysis and chemical profile measurements (Fig. 5) shows a uniform distribution of gold at the surface of magnetite. It is interesting to note that Au(III) can be reduced to Au^0 even by bare Fe_3O_4 MNPs. However, this process leads to the formation of ca. 40-50 nm Au^0 NPs dispersed in Fe_3O_4 matrix (Fig. 6) rather than uniform Au^0 deposition at magnetite surface. Similar results have been obtained in the presence of

ascorbic acid and tryptophan indicating a crucial role of L-cysteine mediation.

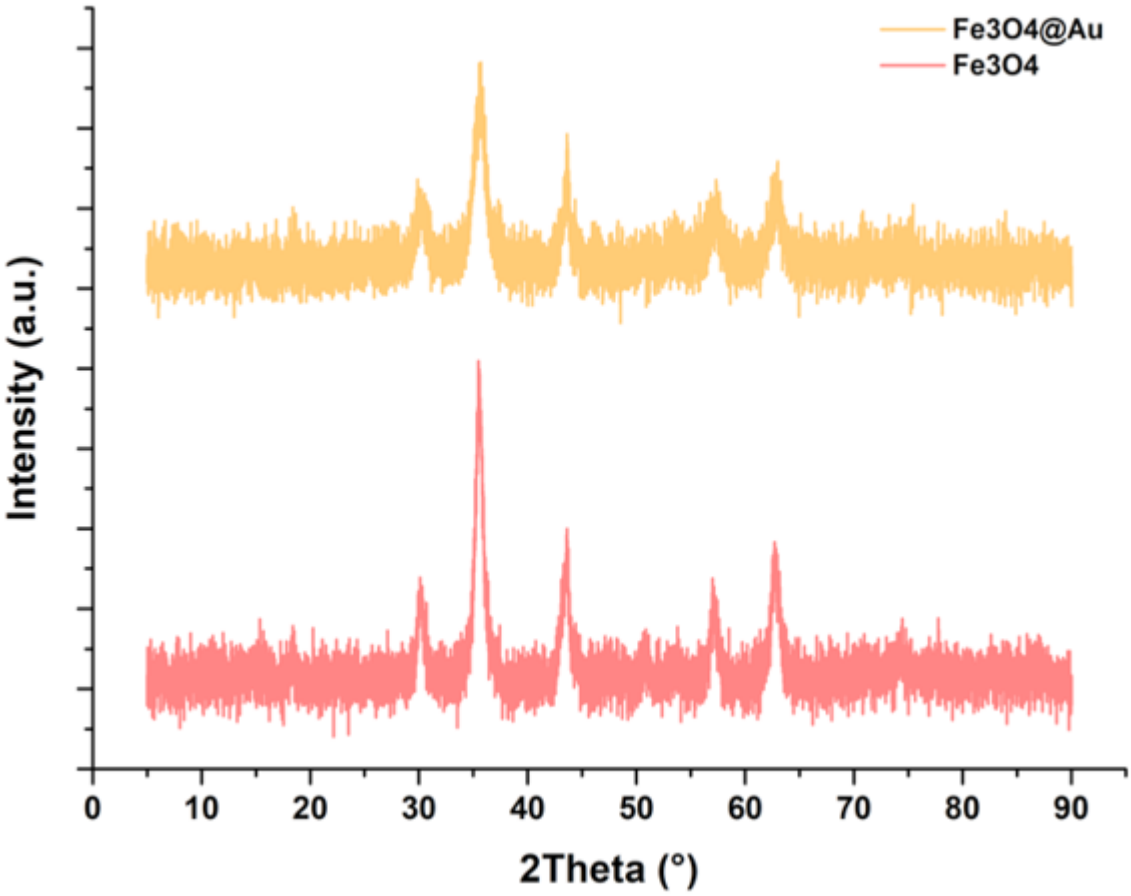

Figure 3: Powder XRD patterns of Fe_3O_4 and Fe_3O_4@Au MNPs.

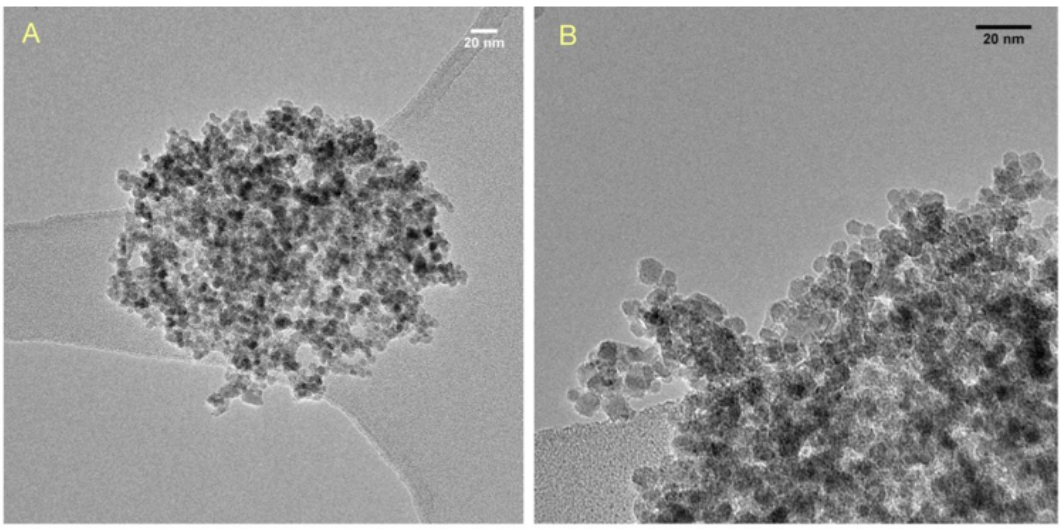

Figure 4: HR TEM of Fe_3O_4@Cys@Au (A&B : scale 20 nm).

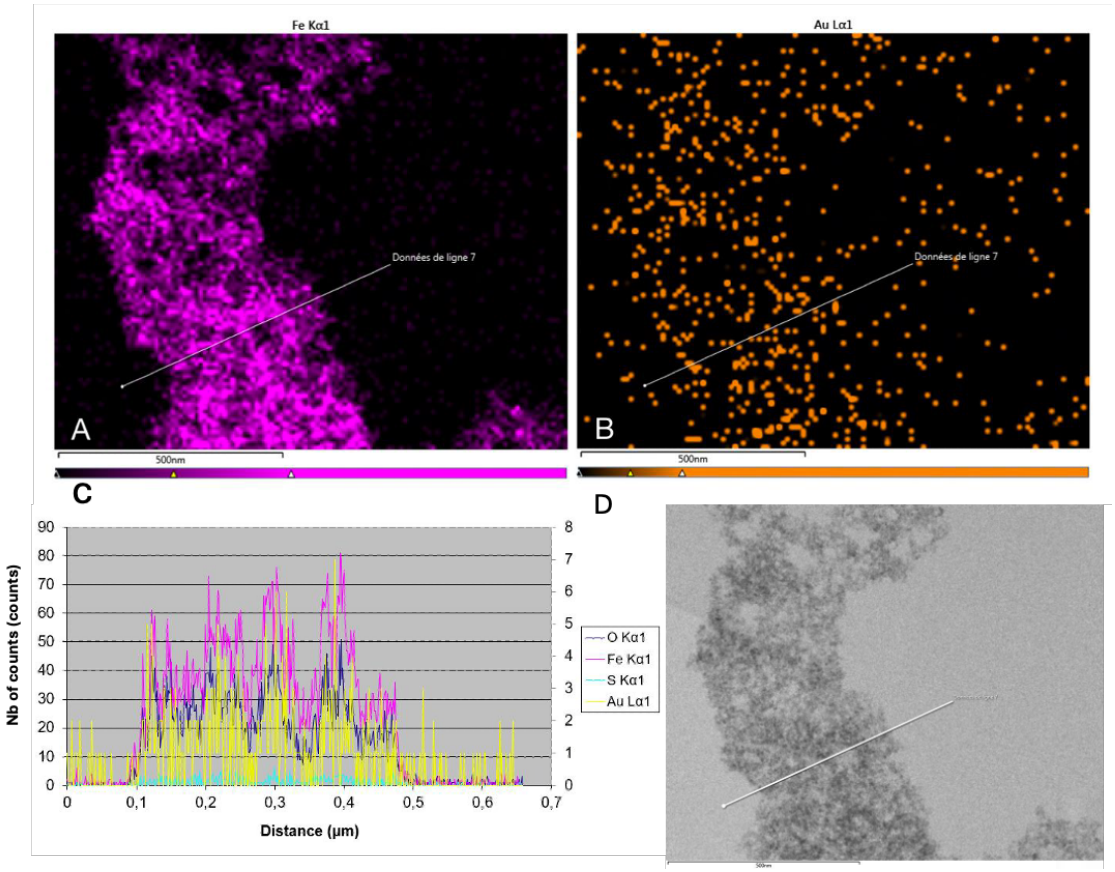

Figure 5: STEM image (D), EDX mapping of Fe (A) and Au (B), and chemical profile (C) of L-cysteine mediated Fe3O4@Au MNPs. The white line corresponds to the scan data of Fig. 5C.

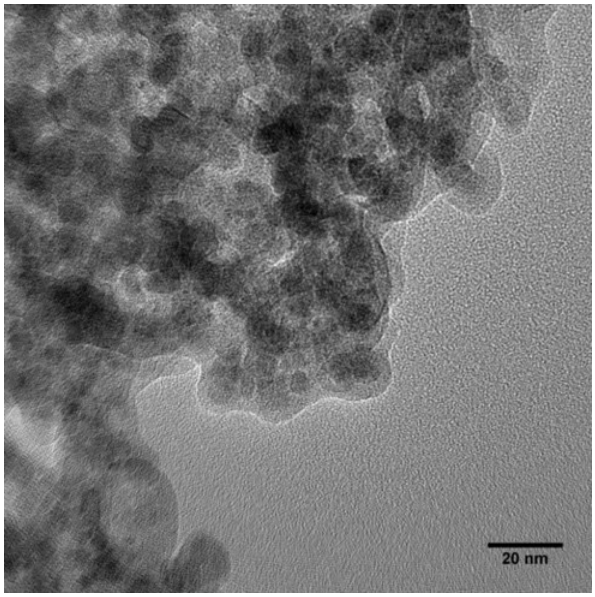

Figure 6 : HRTEM of Fe_3O_4@Au MNPs.

Table 1 summarizes SEM/EDX analysis of L-Cysteine mediated Fe_3O_4@Au MNPs reveling the presence of about 4.5 mass. % of Au and notable amounts of C and S in addition to O and Fe. The presence of C and S points out that the organic binder remains at the surface of magnetite after gold deposition.

Element*	C	O	S	Fe	Au
mass. %	5,3 ± 3,2	25,3 ± 1,8	1,24 ± 0,06	62,9 ± 2,5	4,5 ± 0,3
*Sample also contains ca. 0.23% of Al and 0.51% of Si most likely originated from glass erosion during Fe3O4 synthesis in alkali solution.					

Table 1: Elemental composition of L-Cysteine mediated Fe3O4@Au MNPs.

The relative surface composition of Fe_3O_4@Au MNPs was assessed with high-resolution XPS spectra shown in Fig. 7. The XPS spectrum of Fe (Fig. 7A) demonstrates the simultaneous existence of Fe2p3/2 (710.68 eV) and Fe2p1/2 (725.18 eV) states, which is close to the standard Fe_3O_4 XPS spectrum [20]. On the other hand, the XPS of Au (Fig. 7B) exhibits two intense peaks at 84.5 eV and 88.3 eV assigned to Au4f7/2 and Au4f5/2 states of metallic gold respectively [21]. These data indicate clearly formation of Au^0 at the surface of Fe_3O_4 MNPs.

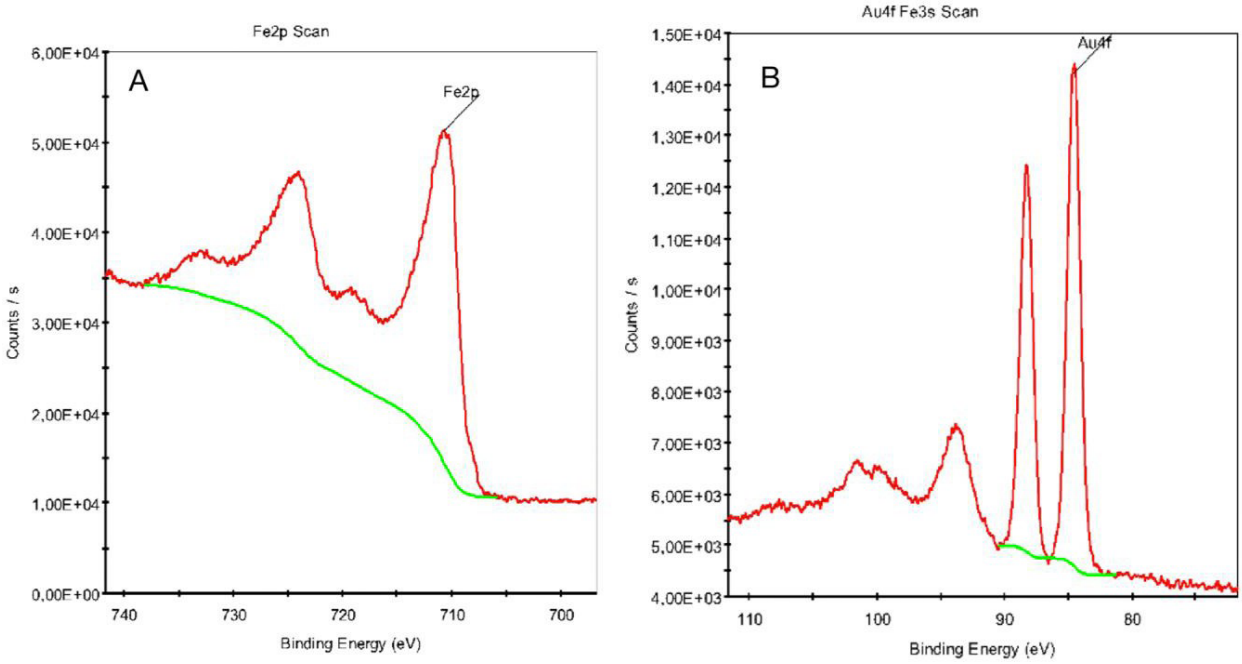

Figure 7: Relative surface composition of Fe_3O_4@Cys@Au MNPs assessed with high-resolution XPS spectra : Fe(2p) region (a); Au(4s) and Fe(3s) region (b)

Physicochemical Properties of the Nanoparticles

Magnetic Properties

At room temperature, Fe_3O_4@Au nanoparticles exhibit ferromagnetism (Fig. 8) with a saturation magnetization (Ms) of 48 emu·g^{-1}, which is comparable to the 51 emu·g^{-1} Ms value of bare Fe_3O_4 nanoparticles recently synthesized through ultrasonically assisted coprecipitation of Fe(II) and Fe(III) in ammonia solutions [17-18].

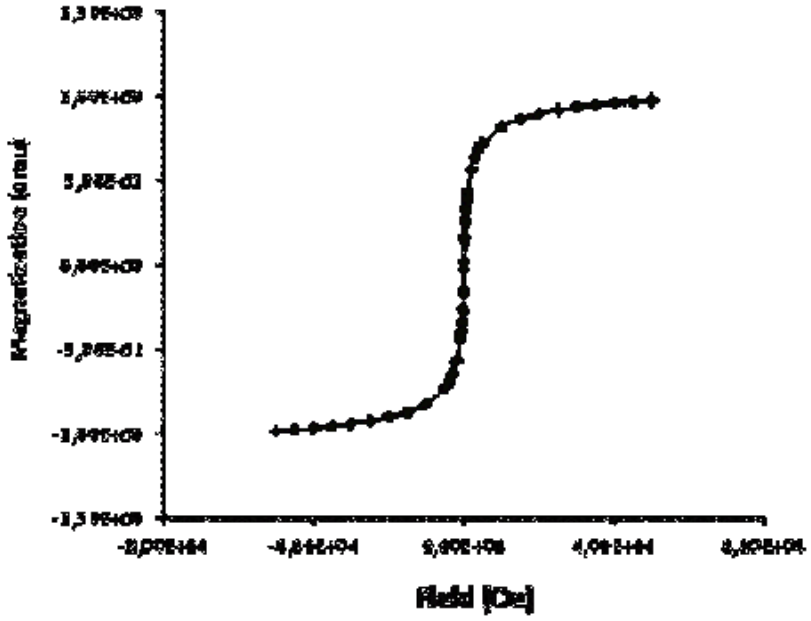

Figure 8: SOUID magnetization curve of 21.0 mg Fe_3O_4@Au nanopowder at room temperature.

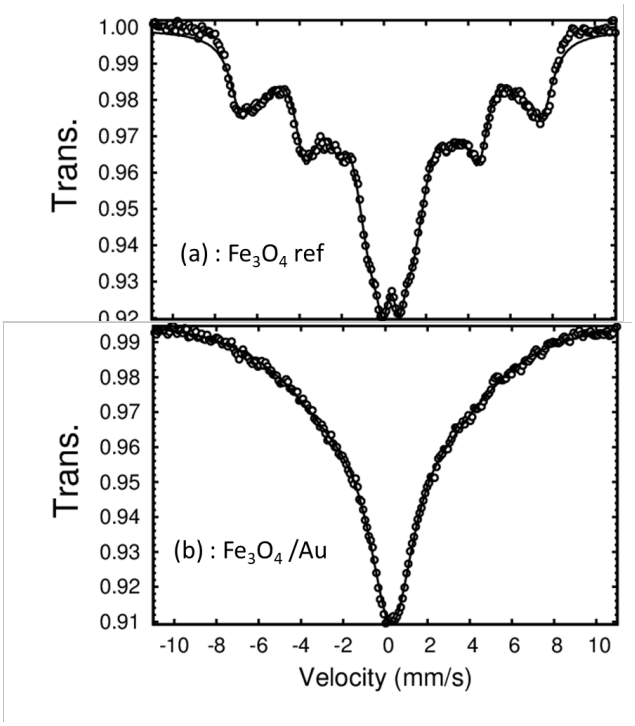

Figure 9: Room temperature 57Fe Mössbauer spectra for bare Fe_3O_4 (A) and Fe_3O_4@Au (B) nanoparticles. Circles: experimental data, solid line: simple fit.

The Mössbauer spectra of bare Fe_3O_4 and Fe_3O_4@Au MNPs (Fig. 5) may be interpreted as a superposition of broad sextet of magnetic phase and broad doublet of superparamagnetic phase. It can be seen clearly that gold coating leads to the increase of contribution of the superparamagnetic phase. It seems to be reasonable to assume that the magnetic phase in the Mössbauer spectrum of bare Fe_3O_4 MNPs is related to the dipole-dipole interaction of magnetic nanoparticles described by the equation (1): [26]

$$V(r) = -V_{max}^2 (r)/6kT \quad (1)$$

where V(r) is an energy of dipole-dipole monodomain attraction, Vmax is a maximal attraction energy in a head-to-tail configuration and r is a distance between the centers of two monodomains. Strong line broadening of the measured Mössbauer spectra confirms the assumption about dipole-dipole interactions. Coating of Fe_3O_4 core with Au^0 shell would increase the distance r and consequently reduce dipole-dipole interaction.

DLS Measurements

In aqueous media, dipole-dipole interactions can lead to aggregate formation.28 Therefore, for theranostic applications it is important to know not only the size of individual magnetic particles but also the size of their aggregates in solutions. Table 2 summarizes the measurements of hydrodynamic diameter of L-Cysteine functionalized Fe_3O_4 and Fe_3O_4@Au MNPs measured using DLS technique. The samples were washed with Milli-Q water followed by magnetic separation. Furthermore, the slurries were dispersed in pure water using ultrasonic bath and filtered through 0.45 μm cellulose filter to remove the largest aggregates. For both materials, particle size distribution curves exhibit only one peak centered around 300 nm, which is much larger than the particle size measured by HRTEM. This effect could be assigned to the dynamic particle association and solvation effect.

Particle	Hydrodynamic diameter (nm)	HRTEM particle size (nm)
Fe3O4/L-Cysteine	290±35	6±1
Fe3O4@Au	322±19	7±1

Table 2: Hydrodynamic diameters of Fe_3O_4/L-Cysteine and Fe_3O_4@Au MNPs in aqueous suspensions with related particle sizes measured by HRTEM. The concentration of particles in aqueous suspensions is about 0.03 mg·mL-1.

Effect of NP on Cell Viability

To assess the cytotoxicity of NP, a cell viability assay was performed. As indicated in Fig. 10, compared with control cells, cells incubated with NP did not present a significant decrease of their viability for a range of concentration from 0.25 mg/ml to 2 mg/ml for 3T3 murine fibroblasts or from 25 to 500 μg/ml for tumor cell lines (MIA PaCa-2 and DU145).

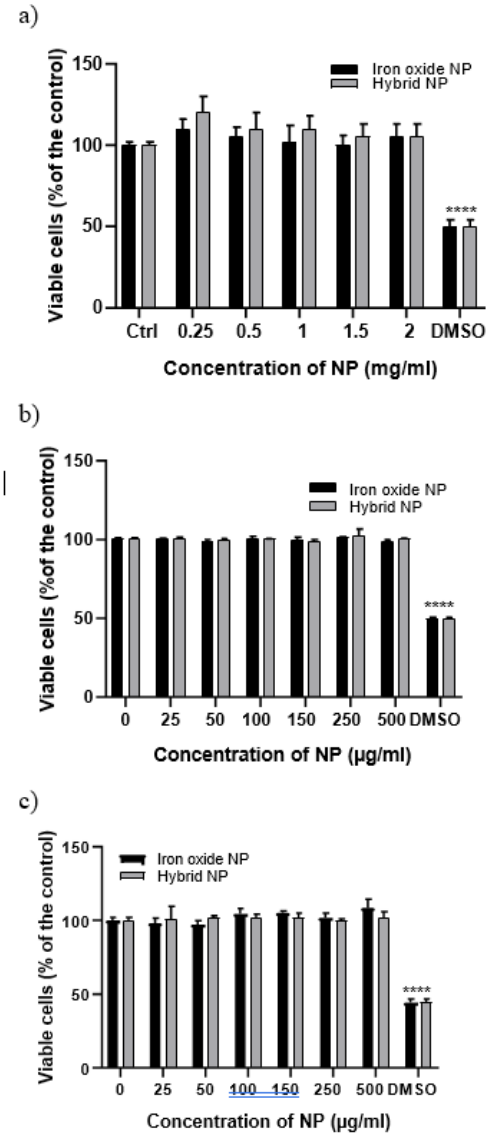

Figure 10: Cytotoxicity. Effects of nanoparticles on a) 3T3 and b) MIA PaCa-2 and c) DU145 cells.

NP enhanced radiosensitivity of pancreatic and prostatic cancer cells

To assess the efficacy of NP as radiosensitizers, a cell viability assay and a clonogenic cell survival assay were performed. As indicated in Fig. 11, the cell viability assay did not show significant

decrease after a 2Gy irradiation at 50 or 100 µg/ml NP. After an irradiation of 4 or 6 Gy, a decrease of the viability was observed. The presence of NP induced a decrease of the viability significantly higher compared to the irradiated control. As shown in Fig. 12, compared with control cells, MIA PaCa-2 cells incubated with NP were sensitized to radiation with a sensitive enhancement ratio (SER) of 1.5 and 1.3 at 2 Gy for hybrid NP and iron oxide NP respectively (Table 1). The same observation was done with DU145 cells with SER of 1.4 and 1.3 at 2 Gy for hybrid NP and iron oxide NP respectively (Table 1). Dose enhancement fractions (DEF) of 1.7 and 1.3 (MIA PaCa-2) or 1.7 and 1.2 (DU145) were calculated from the clonogenic assay results when hybrid NP or iron oxide NP were incubated for 1 hour before irradiation. Both the radiation dose inducing 50% survival (D50%) and the survival fraction at 2 Gy (SF2) decreased in the presence of NP, and this decrease is slightly higher with hybrid NP. In addition, the presence of NP strongly increased the directly lethal damage (α factor).

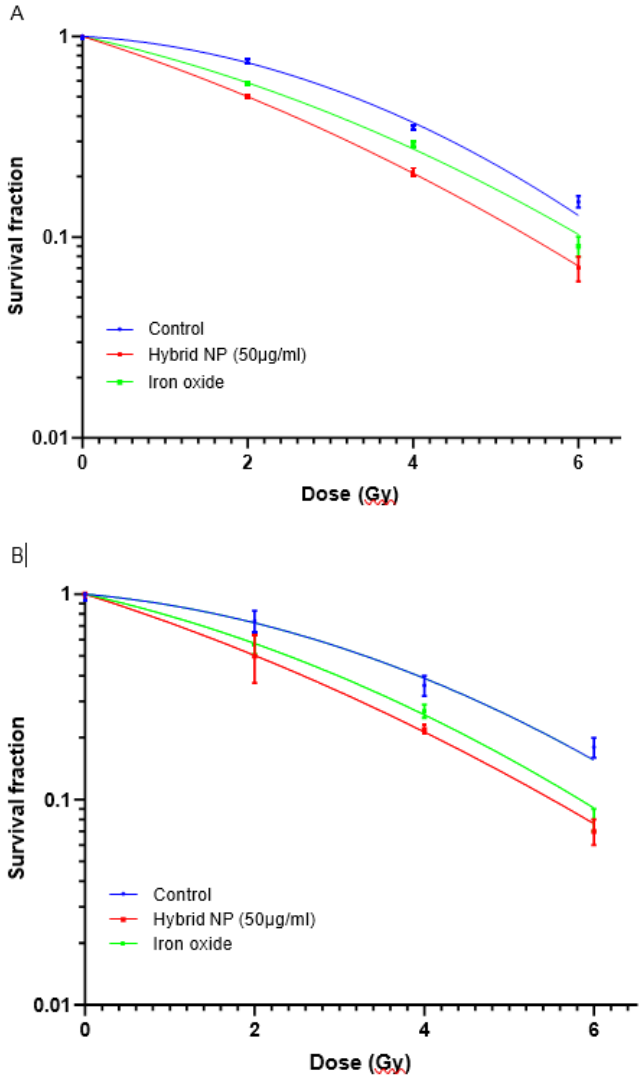

Figure 11: Clonogenic assay. Surviving fraction of MIA PaCa-2 (A) and DU145 (B) cells after radiation exposure without nanoparticles (blue), with incubation with 50µg/ml Hybrid NP (red) and with incubation with 50µg/ml iron oxide NP (green) 1 hour prior to irradiation with 6MV X-ray. Regression analysis was used to fit the data to a linear quadratic model of the form log (SF) = a x D + ß x D^2 (n = 9/point).

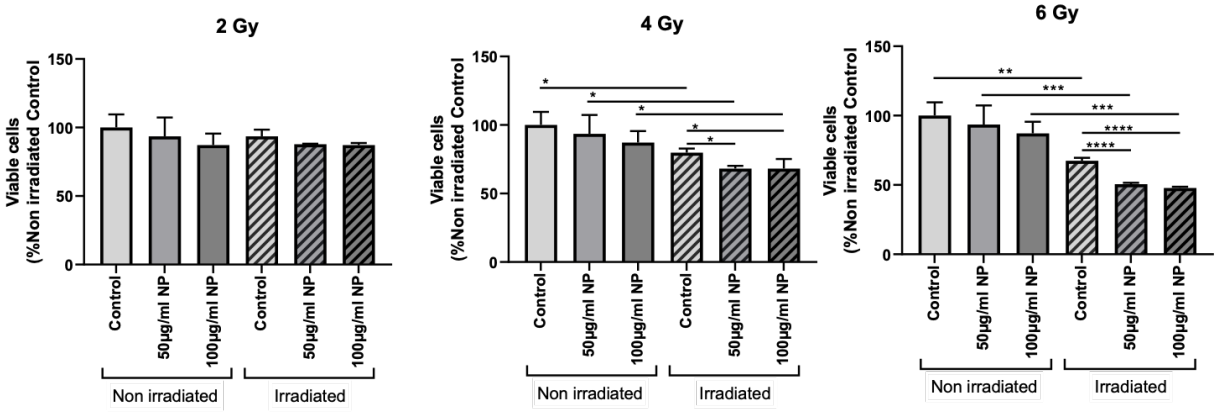

Figure 12: Effects of nanoparticles on cell viability with or without 2, 4 or 6 Gy irradiation. Data are representative of three independent experiments and expressed as mean?SD (n=3, technical replicates).

NP increased the production of ROS and the apoptosis level.

We used the fluorescent probe H2DCFDA to detect the ROS level in living cells. The results showed that the presence of NP significantly increased the ROS level especially when they were irradiated (Fig. 13).

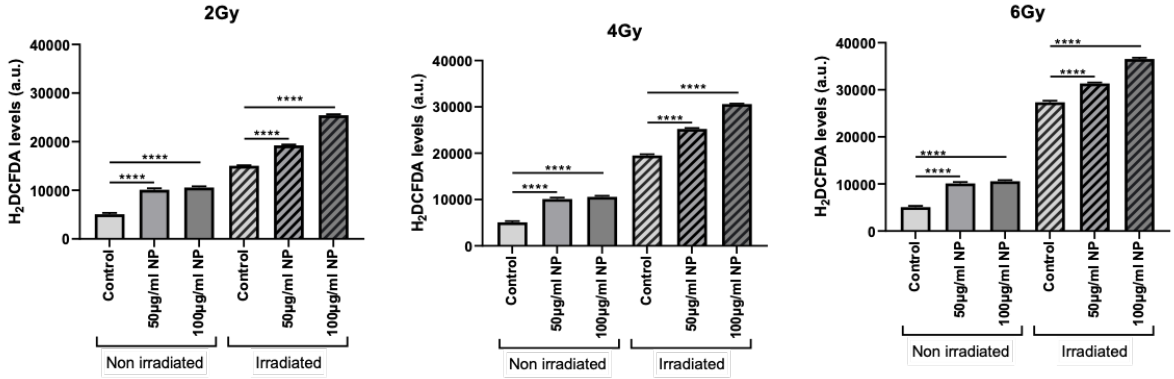

Figure 13: ROS Measurements. Effects of nanoparticles on ROS production in DU145 cells with or without 2, 4 or 6 Gy irradiation. Data are representative of three independent experiments and expressed as mean?SD (n=3, technical replicates).

To assess the effect of NP on cell death, a measurement of apoptosis was performed. In absence of irradiation, the level of apoptosis was like the control, which confirmed the results of the viability assay. When irradiations were performed, the level of apoptosis increased in dose dependent manner and the apoptosis level were significantly higher in the cells exposed to NP compared to the irradiated control (Fig. 14).

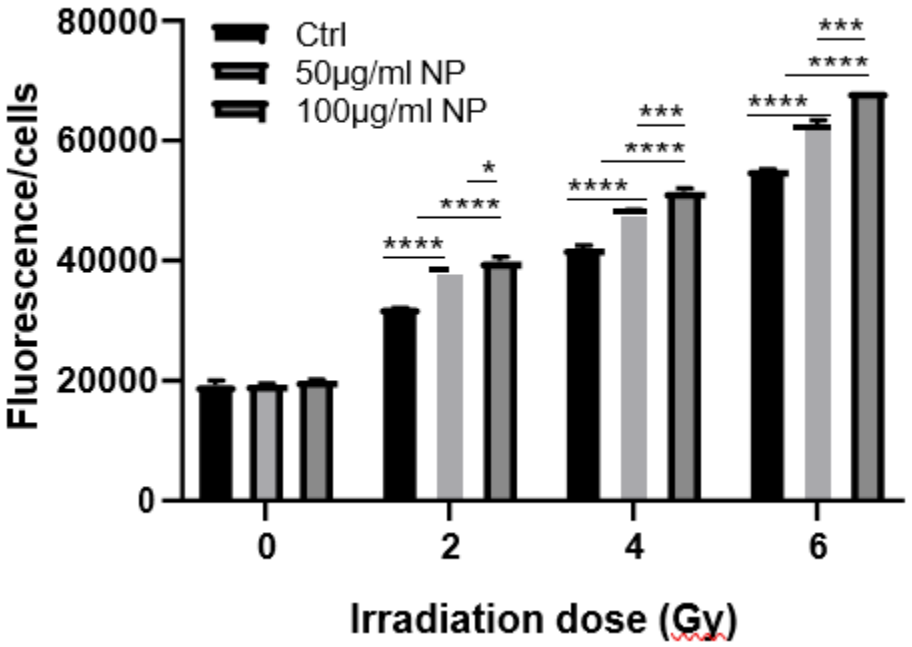

Figure 14: Apoptosis Detection. Quantification of fluorescence intensity in DU145 cells treated with NP with or without RT by Apo-ONE® Homogeneous Caspase-3/7 Assay. Data are mean±SD.

These results suggested that NP combined with X-ray irradiation could increase ROS production in tumor cells to achieve a stronger killing effect.

NP as MRI Contrast Agent

We observed exponential recovery of signal with TR increasing in all T1 curves, and exponential decay of signal with increasing of TE in all T2 curves with both nanoparticles. T1 relaxation time decreased from 1.613 s and 1.826 s for the lowest concentration (0.1 mM) to 0.664 s and 0.941 s for the highest one (1 mM) for iron oxide and hybrid nanoparticles respectively. The T2 relaxation time were from 0.0557 s and 0.0842 s to 0.0123 and 0.024 s for the lowest and the highest concentration and for iron oxide and hybrid nanoparticles respectively.

According to Fig.15, a linear correlation was observed between the relaxation rates (1/T1 and T/T2) and iron concentration allowing to determine r1 and r2. For iron oxide nanoparticles, r1 was 0.98 ± 0.04 mM-1s-1 and r2 was 66.6 ± 6.2 mM-1s-1 which led to the T2/T1 relaxivity ratio of 67.96, and for hybrid nanoparticles r1 was 0.6 ± 0.02 mM-1s-1 and r2 was 34.3 ± 1.8 mM- 1s-1 which led to the T2/T1 relaxivity ratio of 57.2.

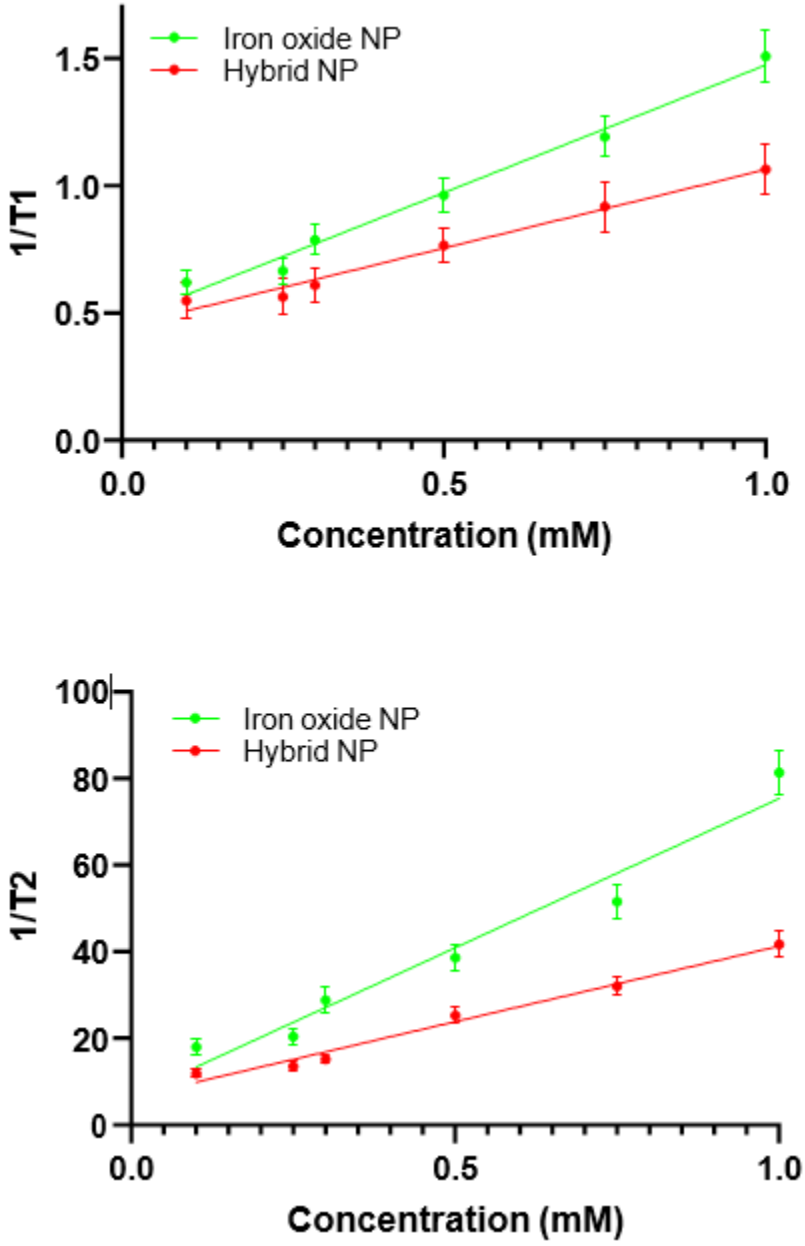

Figure 15: Properties as contrast agent for MRI. Relaxivity (1/T1) and (1/T2) plotted as a function of iron oxide concentration.

Biodistribution Study of NP

Three different nanoparticles were prepared and injected into animals: gold nanoparticles functionalized with neurotensin (Au@NT); and hybrid magnetic nanoparticles coated with neurotensin (Fe_3O4@Au@NT), AMD 3100 (Fe_3O_4@Au@AMD3100).

We did not observe gold in tissue collected from animals having received the magnetic hybrid nanoparticles, despite the fact that the nanoparticles were internalization (Fig 16). We assume that the gold concentration is very low and appears below the limit of quantification (LOQ) of Au obtained by ICPMS, i.e. <1.2ppm. Indeed, the total amount of gold in the hybrid nanoparticles is 4.5%.

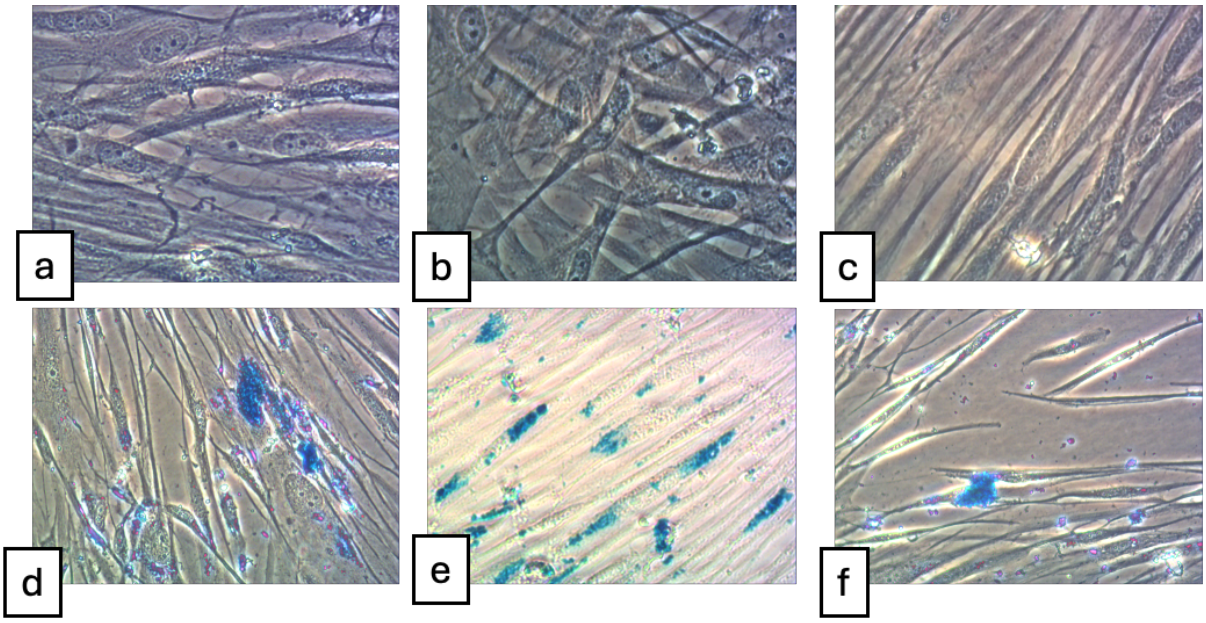

Figure 16: a), b) et c) cells + Prussian blue after 10 , 20 et 30 minutes.

d), e) et f) cells + hybrid NP (24h) + Prussian blue after 10 , 20 et 30 minutes.

Fig 17 a and b show the biodistribution of gold nanoparticles after a) intratumoral or b) intravenous injection. Gold concentration is measured by ICPMS at 1h, 24h and 168h in liver, kidney, plasma, spleen and tumor.

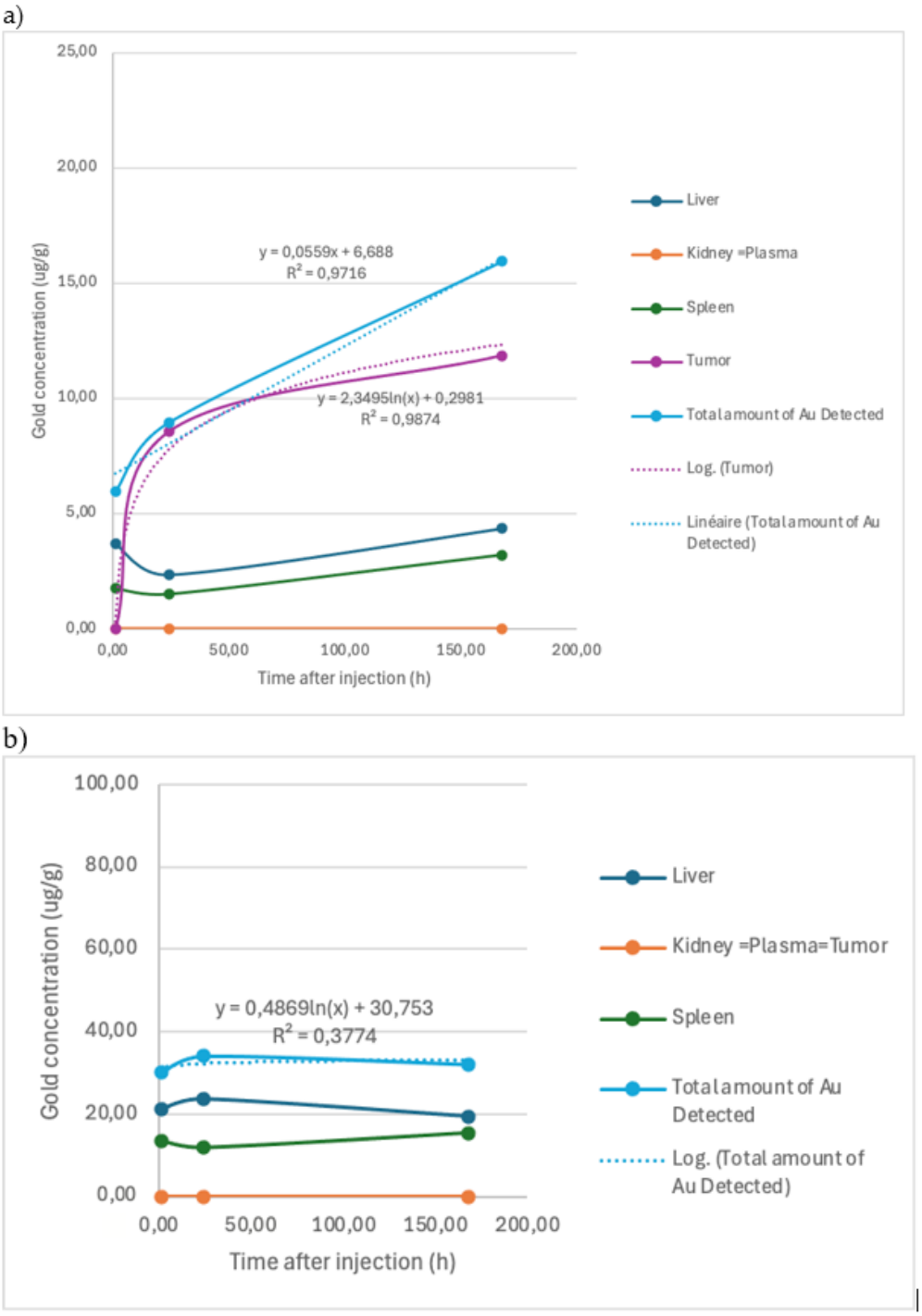

Figure 17: Biodistribution of gold nanoparticles by measuring Au concentration by ICPMS after a) intratumoral or b) intravenous injection.

No gold is significatively measured in kidney and plasma regardless the route of administration, neither in tumor after IV injection. Considering the LOQ and the highest dilution during the IV injection, the nanoparticles are weakly detected in kidney and plasma.

In Fig 17a, the total amount of gold detected after intratumoral injection represents 24% of the initial dose at 1h post injection, 36% at 24h and 64% at 168h.

1h post injection, 92% of the total amount of gold is detected in liver and spleen; at 24h the total amount of Au in tumor reaches 96%, then 74% in tumor at 168h.

Note that the total amount of gold is increasing both in spleen, liver and tumor to reach 64% of the initial dose injected.

The total amount of gold detected regardless the organs follows a linear curve : y = 0,0559x + 6,688

The gold content in tumor follows a log curve : y=2,3495 ln(x) + 0,2981

By calculation, we obtained the maximum of gold detected In vivo (y=25ug/g) at 327.58h, i.e.13.65 days.

These results suggest planning an optimized irradiation of tumor at 14 days. This is in correlation with previous efficacy study on gold nanoparticles for the treatment of skin cancers which consisted in administrating two doses of NP followed by NIR illumination inducing PPTT at 14 days apart [34].

In Fig 17b, the total amount of gold detected after intravenous injection represents 30% of the initial dose at 1h post injection, 34% at 24h and 32% at 168h. Gold is mainly found in spleen and liver. In the tumor, Au remains below the LOQ.

The gold content follows a log curve: y=0.4869 Ln(x) + 30.753

Discussion

Physicochemical Properties of Nanoparticles

The Ms value of hybrid nanoparticles observed in this study is nearly half that of micrometer- sized magnetite [24]. This significant reduction in magnetization cannot be solely attributed to the 4.5% mass of gold on the Fe_3O_4 nanoparticle surface. Instead, it may be explained by increased thermal fluctuations near the magnetite surface and magnetic disorder at the particle surface due to interactions with coordinated L-Cysteine. Notably, these effects become more pronounced as particle size decreases [25]. Additionally, the Fe_3O_4@Au magnetic nanoparticles exhibit very low coercivity (Hc = 6 mT), close to the theoretical value for superparamagnetic particles (Hc = 5 mT) [17], indicating that the Fe_3O_4 particles are close to the size of a magnetic monodomain.

Suggested Mechanism of Gold Coating

L-Cysteine is a fundamental amino acid where the thiol and amino carboxylate groups enable coordination to metallic and metal oxide surfaces. As it was mentioned above, coordination of L-Cysteine onto the surface of bare Fe_3O_4 occurs by bidentate carboxylic group and accompanied by surface reduction of Fe(III) to Fe(II) followed by Cystine formation via S-S binding [22]. On the other hand, Au(III) ions formed strong complexes with sulfide and thiol ligands and can be readily reduced by these groups to Au^0 [23]. Therefore, addition of Au(III) salt to the aqueous suspensions of Fe_3O_4 MNPs with adsorbed Cystine would lead to Au(III) reduction specifically at Fe_3O_4 surface leading to the uniform Au^0 shell bonded to the metal oxide via interaction with organic mediator. In this term, the washing of Fe_3O_4/L-Cysteine particles prior Au(III) addition is an important stage because the excess of L-Cysteine in solution would provide Au^0 formation in the bulk solution and not at the Fe_3O_4.

NP Enhanced Radiosensitivity of Pancreatic and Prostatic Cancer Cells

The ferromagnetic hybrid Fe_3O_4 presents superparamagnetic property at room temperature. We decided to study the dose enhancement in radiotherapy because this is the standard of care to treat pancreatic and prostatic cancers.

The development of nanoparticles interacting with X-rays radiation during radiotherapy is a solution to improve the therapy while sparing the healthy surrounding tissue in deep organ treatment strategy. Among the agents able to enhance the radiation dose, materials like iron oxide and gold can be used. As iron oxide can also be used as MRI contrast agent, we developed iron oxide nanoparticles coated with gold, combining the properties of low toxicities inherent to gold, and the radiosensitizer brought by iron. In this study, we demonstrated that hybrid nanoparticles were not cytotoxic on two cancer cell lines (MIA PaCa-2 and DU145) and were able to increase the sensitivity of these cell lines to radiation. Indeed, a DEF of 1.7 was calculated from the clonogenic assays. This radiosensitization was correlated to the enhancement of ROS production and to the increase of apoptotic cells [27]. Nanoparticles made with a different metal: hafnium oxide, already demonstrated the feasibility and the efficacy of this types of radioenhancers in patients [29-30].

Similar approach of hybrid nanoparticles synthesis reported the use of gadolinium oxide nanoparticles coated with gold as radiosensitizer for the treatment of breast cancer in a murine model. The inhibition of the tumor growth was observed by the combination of radiotherapy and hybrid nanoparticles [31]. Other hybrid gold nanoparticles [32] have been studied as radioactive agent (198Au) and demonstrated good results.

NP as MRI Contrast Agent

The results indicate that both nanoparticles have effects on T1 and T2 relaxation times shortening, but T2 shortening effect is dominant. The relaxivity ratio determines the efficiency of a product as an MRI T1 or T2 agent. If T2/T1 ratio is much higher than 1, the contrast agent will be described as a T2 agent, but if the ratio is closed to 1, the agent will be described as a T1 agent [33]. The high ratio for both nanoparticles confirms that they can act as MRI T2 contrast agent. The ratio is smaller for hybrid NP compared to iron oxide nanoparticles due to the gold presence but the performance as contrast agent is still correct. So, hybrid nanoparticles could increase the sensitivity to radiations and could be used as MRI contrast agent for tumor delineation.

Biodistribution

In this article, we present the sustainable synthesis of hybrid nanoparticles composed of an iron oxide core and a gold shell, namely Fe_3O_4@Au, as a more biocompatible nanoparticle than iron oxides one for which were reported adverse effects observed as MRI contrast agents (SPIO). The functionnalized nanoparticles were injected intravenously and intratumorously into mice model bearing pancreatic cancer. We assume that the use of hybrid NPs coupled with RT would a) potentiate the effects of X-rays thus reducing the radiation dose while allowing the protection of the surrounding healthy tissues or b) deliver a higher dose to the tumor site by emitting the same dose of X-rays.

Hybrid nanoparticles and gold nanoparticles were functionalized with neurotensine and AMD 3100 to target respectively the NRT1 receptors overexpressed in pancreatic cancer cells, and the CXCR4 receptors overexpressed in tumoral stroma. The action of AMD3100 on tumoral stroma consists in disrupting the CXCR4/CXCL12 interaction, which finally affects interactions between tumour cells and stromal cells, thereby reducing the protection offered by the tumour stroma against treatments. This approach leads to a leaky stroma.

The biodistribution of metallic nanoparticles was studied after a) intratumoral injection or b) intravenous injection and monitored by ICPMS by the gold content in liver, kidney, plasma, spleen and tumor.

The strategy consists in 1) degrading the stroma matrix by PPTT for the improvement of chemotherapy and radiotherapy 2) by penetrating the protective layer of the pancreas. Makino and al. [35] reported the biodistribution of pegylated gold nanoparticles as a function of size with a major hepatosplenic and lung captation for 15 and 50nm size nanoparticles. For 15 nm size, major accumulation was detected in liver, lung kidney, brain and spleen. For 50nm size, trace concentration of gold was detected in brain, heart, kidney, pancreas, and stomach, but no observation of gold in blood. When increasing the size to 50nm, we observe a higher accumulation in spleen in comparison with 15nm size NP.

The biodistribution results of the hybrid magnetic nanoparticles present the same profile as the 50nm size pegylated gold nanoparticles described by Makino and al. The physicochemical characterization of the nanoparticles by TEM and DLS reports a size distribution centred around 15nm (in Fig 18) but showing 50nm as average hydrodynamic diameter. This latter measurement obtained by DLS is relevant to better understand the biodistribution and safety profiles of metallic nanoparticles.

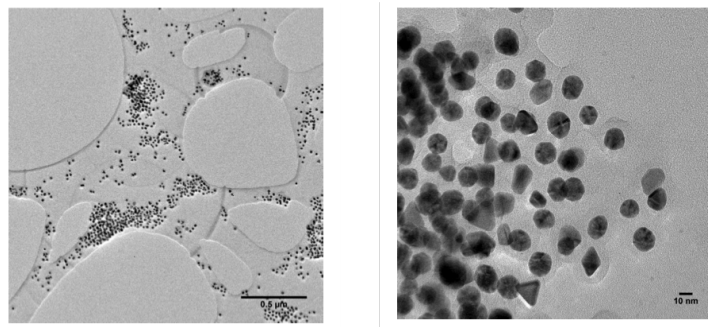

Figure 18: TEM images show quite monodispersed Au nanoparticles with quasi round shape. Some particles are rhombohedral or triangle shaped. The average particle size is 15-25 nm.

Conclusions

We presented an ultrasound-based synthesis of ferromagnetic hybrid nanoparticles. First, the Fe_3O_4 core coated with gold shell presents interesting ferromagnetic properties with characteristics of superparamagnetic Fe_3O_4 core (its coercitivity) that we can interpret as the reduction of dipole dipole interaction caused by the presence of gold.

The use of L cysteine is a solution to stabilize gold at the surface of the iron oxide core. We manage to monitor the quantity of gold deposited by varying the time of cysteine incubation. The aim was 1) to produce in an ecofriendly process the magnetic nanoparticles; 2) design a nanotheranostic agent combining the medical imaging property (MRI) and the therapeutic property for a deep destruction of tumor cells using RT and PPTT.

We have demonstrated the in vitro preclinical efficacy of iron oxide nanoparticles coated with gold as a radiosensitizer. The combination of these nanoparticles with radiation therapy induced significant in vitro dose enhancement on two tumor cell lines: pancreatic (MIA PACA 2) and prostatic cells (DU145). Considering the properties of imaging and therapy, results demonstrate that these newly prepared hybrid nanoparticles could be a good nanotheranostic candidate acting as MRI T2 contrast agent and

radiotherapy enhancer on pancreatic and prostatic cancers. These radiosensitizer characteristics allow the use of CyberKnife® as stereotaxic radiotherapy to better delineate the region of interest.

The metallic nanoparticles, gold and hybrid core shell, were injected into animal model bearing pancreatic cancer to study their preclinical in vivo biodistribution. Two different biomolecules Neurotensin & AMD3100 were respectively used to degrade the stroma cells by PPTT then facilitating the targeting of pancreatic tumor cells. The biodistribution profile of hybrid nanoparticles was not studied because of the low concentration of gold that was not able to be detected by ICPMS. The profile of gold showed a major hepatosplenic captation both by IV or IT at 1h post injection. The trend was reversed at 24h post injection by IT where we could detect gold in tumor.

Finally, the strategy herein presented supports our intent to 1) generate holes by applying the photothermal ablation in stroma allowing 2) the deep penetration of chemotherapy through the neurotensin functionnalized nanoparticles. This concept in two steps would promote the nanoparticles as nanoplatform that once functionalized, could vectorize any conventional chemotherapy combined with the physical therapy, i.e. PPTT, radiotherapy. We also raised the issue of in vivo detection of metallic nanoparticles when they are injected in low but efficient dose even at this level of concentration.

Author Contributions: Conceptualization, A.L.M. and S.N.; methodology, T.C. and S.P.; validation, A.L.M., S.N.; writing—original draft preparation, A.L.M., T.C.; writing—review and editing, A.L.M., T.C.; supervision, A.L.M. and S.N.; project administration, A.L.M.; funding acquisition, A.L.M.

All authors have read and agreed to the published version of the manuscript.

Funding: This research was partially funded by the French Ministry of research (CIR), FEDER and regional council La Réunion island, Torskal nanoscience SAS and Suzhou Anne Gold Nano Biotechnology Co., LTD.

Acknowledgments: A.L.M. and S.P. are grateful to Dr Youssef Slama from Clinifutur health group for having given the access to the accelerator. S. I. N., T. C., and A. G. are grateful to Torskal nanoscience for the financial support. The authors thank V. Flaud, C. Reibel, and M. Sougrati from the University of Montpellier for their help in XPS, SQUID, and Mössbauer measurements. The authors thank Suzhou Anne Gold Nano Biotechnology Co., LTD for the financial support of the biodistribution study. We thank Wuxiapp for the biodistribution study and detection.

Conflicts of Interest: The authors declare no conflict of interest.

Declaration of Interests

The authors declare that they have no known competing financial interests or personal relationships that could have appeared to influence the work reported in this paper.

The authors declare the following financial interests/personal relationships which may be considered as potential competing interests:

Anne-Laure Morel reports financial support was provided by Torskal. Serguey Nikitenki, Tony Chave, Anne-Laure Morel has patent Ultrasonic-assisted synthesis of nanoparticles consisting of a gold covered ferric core pending to Morel, Anne-Laure, Serguei Nikitenko, Tony Chave. If there are other authors, they declare that they have no known competing financial interests or personal relationships that could have appeared to influence the work reported in this paper.

References

1. Spiers F W (1949) The influence of energy absorption and electron range on dosage in irradiated bone. The British journal of radiology 22:521-533.
2. Castillo M H, Button T M, Doerr R, Homs M I, Pruett C W, et al. (1988) Effects of radiotherapy on mandibular reconstruction plates. American Journal of Surgery 156:261-263.
3. Matsudaira H, Ueno A M, Furuno I (1980) Iodine contrast medium sensitizes cultured mammalian cells to X rays but not to ? rays. Radiation research 84:144-148.
4. Hainfeld J F, Dilmanian F A, Slatkin D N, Smilowitz H M (2008). Radiotherapy enhancement with gold nanoparticles. Journal of pharmacy and pharmacology 60:977- 985.
5. Hunstad D A, Norton J A (1995) Management of pancreatic carcinoma. Surg Oncol 4:61-74.
6. Hainfeld JF, Slatkin DN, Smilowitz HM (2004) The use of gold nanoparticles to enhance radiotherapy in mice. Physics in medicine and biology 49:N309-15.
7. Lux F, Sancey L, Bianchi A, Cremillieux Y, Roux S, et al. (2015) Gadolinium-based nanoparticles for theranostic MRI-radiosensitization. Nanomedicine 10:1801-15.
8. Kotb S, Detappe A, Lux F, Appaix F, Barbier E, et al. (2016). Theranostics 6:418-27.
9. Dubey P, Sertorio M, Takiar V (2022) Therapeutic Advancements in Metal and Metal Oxide Nanoparticle-Based Radiosensitization for Head and Neck Cancer Therapy. Cancers 14:514.
10. Li W B, Stangl S, Klapproth A, Shevtsov M, Hernandez A, et al. (2021) Application of High-Z Gold Nanoparticles in Targeted Cancer Radiotherapy-Pharmacokinetic Modeling, Monte Carlo Simulation and Radiobiological Effect Modeling. Cancers 13:5370.
11. Zou W, Liu Z, Wang N, Chen X, Sun X, et al. (2022) Hafnium-Based Metal-Organic Framework Nanoparticles as a Radiosensitizer to Improve Radiotherapy Efficacy in Esophageal Cancer. ACS Omega 7:12021-29.
12. Das P, Fatehbasharzad P, Colombo M, Fiandra L, Prosperi D (2019) Trends Biotechnol 37:995-1010.

13. Sanavio B, Stellacci F (2017) Recent advances in the synthesis and applications of multimodal gold-iron nanoparticles. Curr Med Chem 24:497–511.

14. Wang L, Park H Y, Lim S I, Schadt M J, Mott D, et al. (2008) Core@ shell nanomaterials: gold-coated magnetic oxide nanoparticles. J Mater Chem 18:2629-2635.

15. Wagener P, Jakobi J, Rehbock C, Chakravadhanula V S K, Thede C, et al. (2016) Solvent-surface interactions control the phase structure in laser generated iron-gold core-shell nanoparticles. Sci Rep 6:23352.

16. Narayanan S, Sathy B N, Mony U, Koyakutty M, Nair S V, et al. (2012) Biocompatible magnetite/gold nanohybrid contrast agents via green chemistry for MRI and CT bioimaging. ACS Appl Mater Interfaces, 4:251-260.

17. A L Morel, S I Nikitenko, K Gionnet, A Wattiaux, J Lai-Kee-Him, et al. (2008) Sonochemical approach to the synthesis of Fe3O4@SiO2 core-shell nanoparticles with tunable properties. ACS Nano 2:847-856.

18. Laure M A, Maroua B H, Serguei N, Tony C (2022) synthèse assistée par ultrasons de nanoparticules constituées d'un cœur ferrique recouvert d'or, Patent FR2200483.

19. S P Schwaminger, P F García, G K Merck, F A Bodensteiner, S Heissler, et al. (2015) Nature of interactions of amino acids with bare magnetite nanoparticles. J Phys Chem C 119:23032-23041.

20. Y Xing, Y Y Jin, J C Si, M L Peng, X F Wang, et al. (2015) Controllable synthesis and characterization of Fe3O4/Au composite nanoparticles. J Magn Magn Mat 380:150-156.

21. L Caprile, A Cossaro, E Falletta, C Della Pina, O Cavalleri, et al. (2012) Interaction of L-cysteine with naked gold nanoparticles supported on HOPG: a high resolution XPS investigation. Nanoscale 4:7727-7734.

22. S P Schwaminger, P F García, G K Merck, F A Bodensteiner, S Heissler, et al. (2015) Nature of interactions of amino acids with bare magnetite nanoparticles. J Phys Chem C 119:23032-23041.

23. I V Mironov, V Yu Kharlamova (2023) On redox processes of gold(III) complexes with biologically important thiols: cysteine, glutathione, thiomalate. Chem Select 8:e202301337.

24. B D Cullity (1972) Introduction to magnetic materials. Addison-Wesley Publishing: Reading, MA, USA, 410-421.

25. J L Viota, J D C Duran, F Gonzalez-Caballero, A V Delgado (2007) Magnetic properties of extremely bimodal magnetic suspensions. J Magn Magn Mater 314:80-86.

26. P C Scholten (1978) In: Thermomechanics of magnetic fluids; B Berkovsky Ed, Hemisphere Publishing Corporation 16-24.

27. Slama Y, Arcambal A, Septembre-Malaterre A, Morel A L, Pesnel S, et al. (2024) Evaluation of core-shell Fe3O4@ Au nanoparticles as radioenhancer in A549 cell lung cancer model. Heliyon 10: e29297.

28. H Iida, K Takayanagi, T Nakanishi, T Osaka (2007) Synthesis of Fe3O4 nanoparticles with various sizes and magnetic properties by controlled hydrolysis. J Colloid Interface Sci 314:274-280.

29. Bagley AF, Ludmir EB, Maitra A, Minsky BD, Smith GL, et al. (2022) NBTXR3, a first-in-class radioenhancer for pancreatic ductal adenocarcinoma: Report of first patient experience. Clin Transl Radiat Oncol 33:66-9.

30. Verry C, Dufort S, Villa J, Gavard M, Iriart C, et al. (2021) Theranostic AGuIX nanoparticles as radiosensitizer: A phase I, dose-escalation study in patients with multiple brain metastases (NANO-RAD trial). Radiotherapy and Oncology 160:159-65.

31. Nosrati H, Salehiabar M, Charmi J, Yaray K, Ghaffarlou M, et al. (2023) Enhanced in vivo radiotherapy of breast cancer using gadolinium oxide and gold hybrid nanoparticles. ACS Applied Bio Materials 6: 784-792.

32. Katti K V, Kannan R, Katti K, Kattumori V, Pandrapraganda R, et al. (2006) Hybrid gold nanoparticles in molecular imaging and radiotherapy. Czechoslovak Journal of Physics 56:D23-D34.

33. Zareei L, Divband B, Mesbahi A, Khatamian M, Kiani A, et al. (2019) A New Potential Contrast Agent for Magnetic Resonance Imaging: Iron Oxide-4A Nanocomposite. J Biomed Phys Eng 9:211-6.

34. Pesnel, S, Bertolotti A, Duquenne S, Zahouani H, Mortier L, et al. (2024). Plasmonic nanophotothermal therapy: Destruction of 500 mm3 subcutaneous human basal cell carcinoma with gold nanoparticles and near infrared laser. Skin Research and Technology 30:e13890.

35. Sonavane G, Tomoda K, Makino K (2008) Biodistribution of colloidal gold nanoparticles after intravenous administration: effect of particle size. Colloids and Surfaces B Biointerfaces 66: 274-280.